High-pressure nuclear inelastic scattering with backscattering monochromatization

Ilya Sergueev,[a]* Konstantin Glazyrin,[a] Markus G. Herrmann,[b] Pavel Alexeev,[a] Hans-Christian Wille,[a] Olaf Leupold,[a] Andrew F. May,[c] Tribhuwan Pandey,[c] Lucas R. Lindsay,[c] Karen Friese[b] and Raphael P. Hermann[c]*

[a]Deutsches Elektronen-Synchrotron DESY, D-22607 Hamburg, Germany, [b]Jülich Centre for Neutron Science-2/Peter Grünberg Institut-4, Forschungszentrum Jülich GmbH, D-52425 Jülich, Germany, and [c]Materials Science and Technology Division, Oak Ridge National Laboratory, Oak Ridge, TN 37831, USA. *Correspondence e-mail: ilya.sergueev@desy.de, hermannrp@ornl.gov

The capability to perform high-pressure low-temperature nuclear inelastic scattering on ^{125}Te and ^{121}Sb with a sapphire backscattering monochromator is presented. This technique was applied to measure nuclear inelastic scattering in TeO_2 at pressures up to 10 GPa and temperatures down to 25 K. The evaluated partial Te densities of phonon states were compared with theoretical calculations and with Raman scattering measured under the same conditions. The high-pressure cell developed in this work can also be used for other techniques at pressures up to at least 100 GPa.

1. Introduction

Nuclear inelastic scattering (NIS) is a technique for studying vibrational modes and phonons in order to investigate the thermodynamic, vibrational and elastic properties of solids (Seto *et al.*, 1995; Sturhahn *et al.*, 1995; Chumakov & Sturhahn, 1999). Because it utilizes nuclear resonant absorption for particular isotopes, it provides element-specific insights for compounds possessing those isotopes. The majority of NIS studies are performed with ^{57}Fe and other isotopes with nuclear resonance energies below 30 keV, such as ^{119}Sn, ^{151}Eu, ^{149}Sm and ^{161}Dy. The development of sapphire backscattering monochromators (BSMs; Shvyd'ko & Gerdau, 1999; Wille *et al.*, 2006, 2010*a*; Sergueev *et al.*, 2011) has opened a route to applying NIS to isotopes with resonance energies above 30 keV, namely ^{121}Sb, ^{125}Te and ^{129}Xe (Klobes *et al.*, 2013). This is beneficial for the study of the many novel functional materials with antimony and tellurium constituent elements. Examples include Fe(Se,Te)-based high-temperature super-conductors (Mizuguchi & Takano, 2010; Ksenofontov *et al.*, 2010), Ge–Sb–Te-based phase-change materials (Wuttig & Yamada, 2007; Matsunaga *et al.*, 2011), and Te- or Sb-based thermoelectrics and topological insulators: binary compounds, *e.g.* PbTe (Bauer Pereira *et al.*, 2013), Bi_2Te_3 and Sb_2Te_3 (Bessas *et al.*, 2012), or complex nanostructured compounds, such as $(AgSbTe_2)_x(PbTe)_{1-x}$ (Snyder & Toberer, 2008). The functional, structural and thermal properties of these materials are related to their phonon structure and resulting phenomena like electron–phonon coupling and anharmonicity.

One of the advantages of NIS is its applicability at high pressure, up to 1 Mbar (1 bar = 100 000 Pa; Zhao *et al.*, 2004). The response of phonon modes to compression provides detailed information on the material's anharmonicity, sound
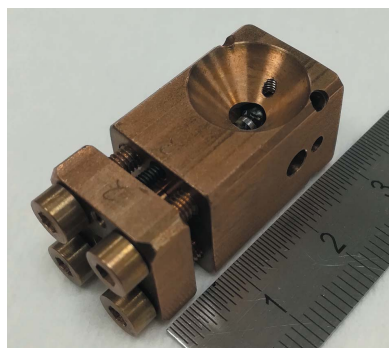
velocity and nonlinear lattice behaviour (Zhang *et al.*, 2013; Parshin *et al.*, 2016; Sergueev *et al.*, 2015). Such studies are important for the synthesis and design of new compounds, as the physical properties can be finely tuned and investigated by modifying the interatomic distances under pressure.

The room-temperature Lamb–Mössbauer factor is extremely small for Sb and Te within most materials as the nuclear resonance energies for the ^{121}Sb and ^{125}Te nuclear isotopes are quite high at 37.1 and 35.5 keV, respectively. This leads to multi-phonon scattering contributions that dominate the inelastic scattering signal and, therefore, prevent the extraction of the one-phonon scattering term and the partial density of phonon states (PDOS). Thus, NIS with these isotopes must be conducted at temperatures generally below 50–100 K, a requirement that also remains valid for high-pressure studies, except at very high pressures (above 50–100 GPa), where the densification of the material ultimately leads to a Lamb–Mössbauer factor increase (Simon *et al.*, 2014). However, scientific interest in many applied materials is focused upon moderate pressures (below 20–30 GPa).

Here, we describe a new capability for high-pressure low-temperature nuclear inelastic scattering, using the 35.5 keV nuclear resonance transition in the ^{125}Te isotope on the Dynamics Beamline P01 at PETRA III (DESY, Hamburg) (Wille *et al.*, 2010*b*). The experimental setup for high-resolution sapphire backscattering monochromatization and beam focusing at the sample position is described in the next section. The miniaturized panoramic diamond-anvil high-pressure cell, which gives access to pressures up to at least 100 GPa, is described in the third section. The fourth section demonstrates the application of the technique to study phonons in TeO$_2$ at pressures up to 10 GPa and temperatures down to 25 K. The last section is devoted to a discussion of possible improvements to the setup and the applicability of the method to the ^{121}Sb nuclear isotope.

2. Experimental setup

The challenge of nuclear inelastic scattering with a sapphire BSM is to provide a reasonable energy resolution, ~1 meV, as required for meaningful studies of phonons. This resolution at energies of 35–40 keV requires an ultra-high-quality monochromator crystal with a lattice spacing variation $\Delta d/d \le 10^{-8}$, where d is the lattice parameter. Topographic investigations of sapphire crystals (Sergueev *et al.*, 2011; Jafari *et al.*, 2017) show that such quality can be reached, but so far only over a limited area with a characteristic size of 0.5 mm. This imposes limitations on experimental setups for which the beam size at the BSM position must then be of the order of 0.5 mm or less.

Another parameter influencing the energy resolution is the angular offset from exact backscattering, $\Delta\theta = \pi/2 - \theta$, where θ is the Bragg angle. The energy resolution near the exact backscattering is defined as $\Delta E/E = [(\Phi\Delta\theta)^2 + (\Delta E_0/E)^2]^{1/2}$, where ΔE_0 is the energy resolution at exact backscattering ($\theta = \pi/2$) and Φ is the divergence of the incoming beam in the scattering plane. For typical values of $E = 35$ keV, $\Phi = 20$ µrad (horizontal beam divergence) and $\Delta E_0 = 0.6$ meV, the effect of

the angular offset on the energy resolution, $\Phi\Delta\theta$, becomes comparable with $\Delta E_0/E$ at $\Delta\theta = 0.05°$. Thus, in order to avoid energy-resolution broadening, $\Delta\theta$ must be less than 0.05°. This limits the gap at the sample position between the beams incident on and reflected from the BSM to ~35 mm, assuming a 20 m longitudinal distance between the BSM and the sample. This restriction cannot be alleviated by decreasing Φ through collimation of the incoming beam because of the requirement to have a small size for the beam impinging on the monochromator crystal, as discussed above. Thus, the sample environment, which is ultimately the pressure cell, must be small in size, at least in the scattering plane, so as to accommodate the two beams.

The small gap between the incident and reflected beams also limits the choice for optical devices that focus the beam at the sample position. Previously, Kirkpatrick–Baez mirrors were used to focus the beam in a high-pressure room-temperature NIS experiment with backscattering monochromatization (Simon *et al.*, 2014). The large size of the device installed ~1 m before the sample requires a large angular offset $\Delta\theta$ and, therefore, led to a significant increase in the energy resolution. Here, we used compound refractive lenses (CRLs) as focusing devices, which provide a reasonable beam size at the sample position over the studied pressure range and do not add additional restrictions on the beam path.

The experimental setup employed for our study on beamline P01 at PETRA III is shown in Fig. 1. At 35.5 keV the undulator beam has a source size of 25 µm × 330 µm (FWHM) and an angular divergence of 10 µrad × 20 µrad (FWHM), vertically and horizontally (V × H), respectively. The beam was monochromated to a bandwidth of 5 eV using an Si(111) double-crystal high-heat-load monochromator (DCM). The beam was collimated in the vertical direction to a size of 0.5 mm using the curvature of the DCM crystals and optimizing the position of the beam on those crystals.

The 34 cylinder parabolic Be CRLs (CRL$_1$), with radii of 0.5 mm and geometric apertures of 1 mm, were installed 67 m from the source in order to focus the beam in the horizontal direction. The beam size at the BSM, 88 m from the source, was ~0.5 mm × 0.6 mm (V × H).

The sapphire crystal, installed in a nitrogen gas-flow cryostat, reflected the beam in the vertical direction with an angular offset of $\Delta\theta = 0.029°$ from exact backscattering. The
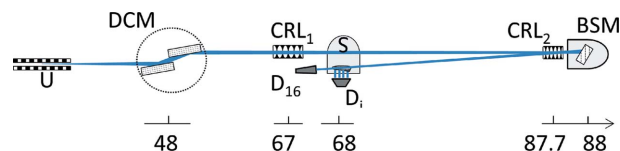
Figure 1
The experimental setup for an NIS experiment on the P01 beamline at PETRA III with undulators (U), a high-heat-load double-crystal monochromator (DCM), horizontal cylinder parabolic Be compound refractive lenses (CRL$_1$), the sample in the cryostat (S), rotationally parabolic Be compound refractive lenses (CRL$_2$), the sapphire back-scattering monochromator (BSM) crystal in the nitrogen gas-flow cryostat and avalanche photodiode detectors (D$_i$, D$_{16}$). The bottom scale shows the distances in metres from the source to the optical elements.

crystal temperature was controlled with millikelvin precision (Alexeev *et al.*, 2016). The position of the beam on the crystal was optimized to achieve the best possible energy resolution.

Nineteen rotationally parabolic Be CRLs (CRL$_2$), with radii of 1 mm (2 mm geometrical aperture), were installed 0.3 m upstream of the BSM. The beam passes through these CRLs in two directions with an offset of 0.3 mm, comparable with the beam size and smaller than the CRL radius. This setup provides an effective duplication of the focusing power without requiring additional lenses and achieves a beam size of 140 μm × 230 μm (V × H) at the sample position.

The nuclear resonance signal was separated in time from electronic X-ray fluorescence and scattering, and measured using two Si avalanche photodiode (APD) systems. An array of 16 APD detectors (D$_{16}$) was installed in the forward direction, with a separation between the electronic scattering and the delayed nuclear resonance scattering signal of 2.5 ns and an absorption efficiency to 35.5 keV of ∼25%. Two 10 mm × 10 mm APD detectors (D$_i$) were installed on both sides, horizontally, close to the sample and detecting mainly the 27.4 keV internally converted nuclear fluorescence that follows the nuclear inelastic absorption process. The separation between the electronic scattering and the delayed nuclear resonance signal for the latter detectors was 5 ns. The absorption efficiency of each detector was ∼7%.

The total flux of the beam between the sapphire BSM and the sample was monitored by a 100 μm-thick Si APD detector which indicated a total flux of 1×10^8 photons s^{-1} at the sample position.

The ^{125}Te nuclear resonance energy was reached using the (9 1 $\overline{10}$ 68) sapphire reflection (in the hexagonal notation). The nuclear resonance signal of the sapphire crystal was observed at a temperature of 217.5 (1) K. The temperature–energy conversion parameter was 0.149 meV mK^{-1} as confirmed by measurement of the NIS spectra on elemental
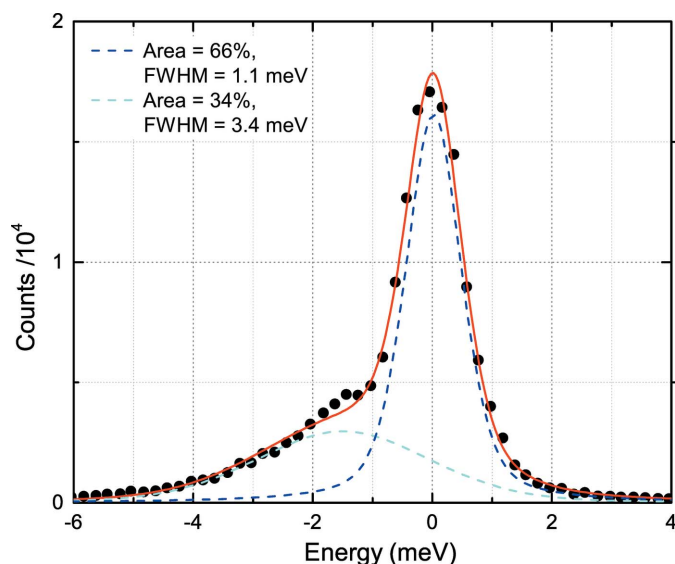
Te. The sapphire BSM instrumental function measured by D$_{16}$ is shown in Fig. 2 and corresponds to a FWHM of 1.25 meV, whereas a 0.6 meV resolution is expected in theory. The function contains an additional satellite peak resulting from defects in the sapphire crystal. Fitting the data by two pseudo-Voigt functions, we obtain areas of 66% and 34% for the main and satellite peaks, with FWHMs of 1.1 and 3.4 meV, respectively.

## 3. Design of the high-pressure cell

The main requirement for the high-pressure cell used in the NIS experiment is the small distance required between the sample and the detectors to increase the solid angle for the 10 mm × 10 mm APD detectors that collect the nuclear fluorescence flux. A system with similar purpose that includes a miniature panoramic diamond anvil cell (DAC) in a cryostat was developed on beamline 3-ID of the APS (Bi *et al.*, 2015; Zhao *et al.*, 2017). However, that system would not fit the backscattering setup reported here because of the requirement to have the path for the incident beam close to the DAC.

Within this work we designed and utilized a new compact piston–cylinder DAC with typical dimensions of 15 mm × 15 mm × 30 mm in the assembled state (see Fig. 3). The technical drawings of the cell were produced at the Jülich Centre for Neutron Science-2, Forschunszentrum Jülich GmbH, Germany (JCNS-2). The cell body (piston–cylinder design), the seats supporting the diamonds, and the screws were manufactured from BeCu alloy at the Bayerisches Geoinstitut, Bayreuth University, Germany.

The distances from the sample position to the three closest faces are 7.5, 7.5 and 8 mm. For compression, the design employs four M3 screws. The cell has several apertures, allowing the incident beam to reach the sample position either in the geometry parallel to the compression axis, *i.e.* through

Figure 2
The instrumental function of the sapphire BSM measured with the nuclear forward scattering of ^{125}Te. The red curve shows a fit to the data with a combination of two pseudo-Voigt profiles.
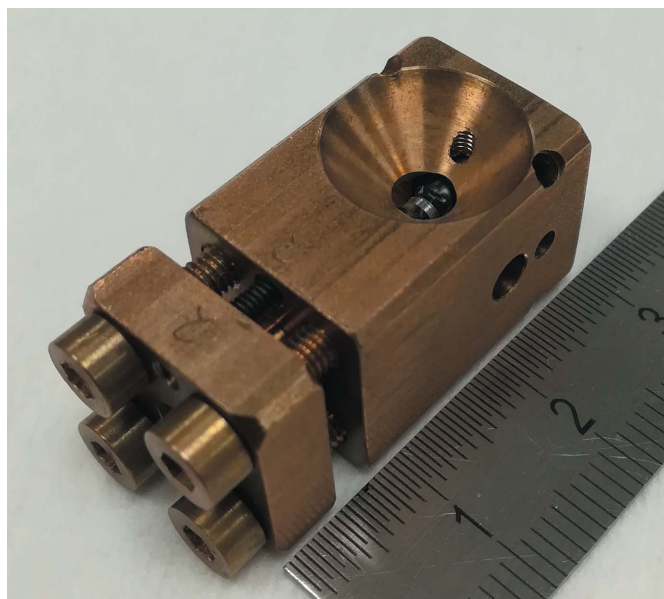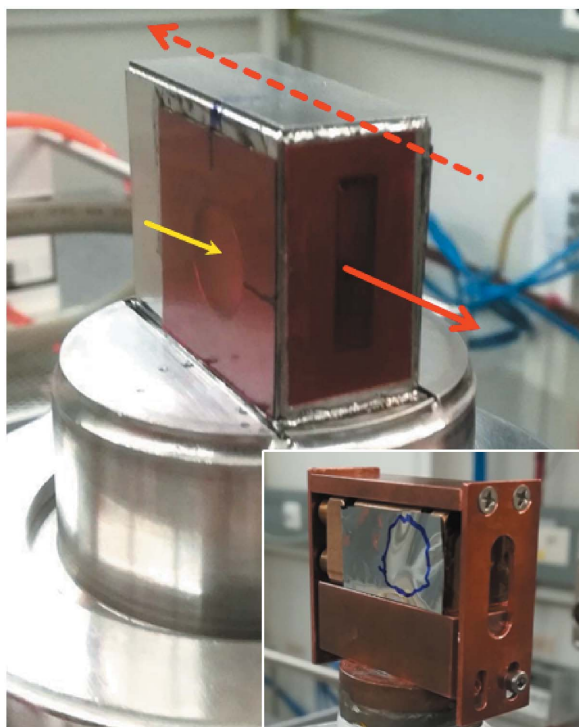

Figure 3
An image of the piston–cylinder DAC employed in this work.

the diamonds, or perpendicular to the compression axis, *i.e.* through an X-ray transparent gasket. For the purpose of NIS signal detection we also implemented a conical aperture of 84° on opposing sides of the cell, namely, perpendicular to the compression axis. The opening created by the intersection of the latter aperture with the inner cylinder enables access for installation of X-ray transparent gaskets (4–5 mm in diameter), as well as sample or pressure-standard loading on the anvil attached to the cell body (cylinder). The rectangular shape of the cell helps us to reach a compromise in several desired features: (i) a minimum sample-to-detector distance, (ii) easy mounting onto flat surfaces, (iii) the possibility to stack several cells, and (iv) a low thermal mass.

While in the current state we cannot increase pressure by means of a gas membrane, this option is foreseen and will be implemented in the future, enabling pressure changes at low temperature.

In addition to the application of the cell to NIS experiments, the chosen design also allows for easy expansion in terms of other available methodologies, such as X-ray emission spectroscopy, X-ray absorption near-edge structure (XANES), extended X-ray absorption fine structure (EXAFS), X-ray diffraction (radial geometry) and Raman scattering.

The DAC stage was mounted in a closed-cycle cryostat as shown in Fig. 4. The cryostat cap was designed and manufactured at JCNS-2. Two APD detectors were installed on the sides in front of the Kapton windows at a distance of 10 mm

from the sample. The beam incident on the BSM passes 20 mm above the reflected beam.

The closed-cycle cryostat produces vibrations of the order of 20–40 μm in the directions along and perpendicular to the beam. They lead to jitter of the beam at the sample position but this is not important for this setup due to the beam size of 140 μm × 230 μm.

The lowest temperature of the closed-cycle cryostat cold finger is ∼10 K. The lowest temperature of the sample is defined by the thermal gradient between the cryostat cold finger and the DAC stage and by the radiation heat-exchanged through the Kapton windows. The thermal contact between the DAC stage and the cold finger in the current work allowed the sample to reach 25 K, as confirmed by the detailed balance of the NIS spectra, see below.
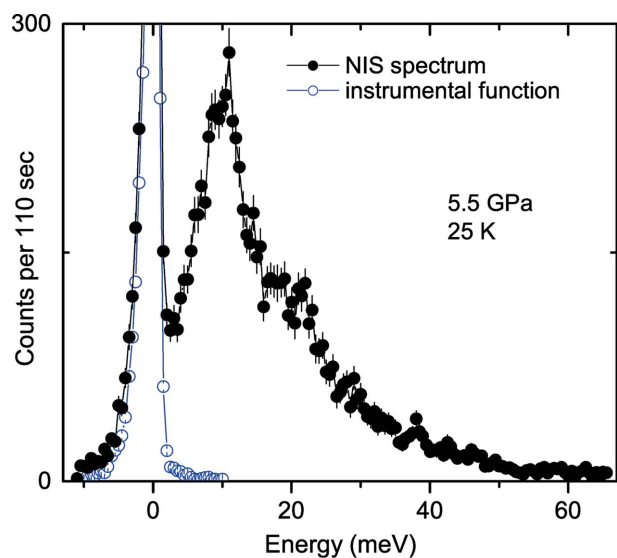
4. High-pressure nuclear inelastic scattering with $^{125}TeO_2$

To demonstrate the capabilities of the above-described method and equipment, we measured high-pressure NIS on $^{125}TeO_2$. TeO_2 has peculiar nonlinear optical and lattice dynamics properties and is utilized for example in acousto-optics (Kondratyuk *et al.*, 1987; Thomas, 1988). At ambient pressure, three polymorphs, α, β and γ, are known for TeO_2. In this study we have utilized α-TeO_2, paratellurite (space group $P4_12_12$, tetragonal phase) (Lindqvist, 1968; Kondratyuk *et al.*, 1987), which is formed by corner-sharing TeO_4 trigonal bipyramids. Under compression it transforms to an orthorhombic phase (space group $P2_12_12_1$) at 0.9 GPa via a second-order transition caused by acoustic mode softening (Worlton & Beyerlein, 1975; Liu, 1987).

Fine-grained polycrystalline TeO_2, prepared by oxidation of 95% ^{125}Te-enriched elemental tellurium, was loaded into a 200 μm hole of the Be gasket, without a pressure-transmitting medium, together with ruby chips used as pressure markers. The initial sample thickness was ∼60 μm. The gasket was mounted into the DAC equipped with 400 μm culet diameter diamond anvils. Measurements were performed at 5.5 (3) and 8.4 (3) GPa and low temperatures.

Pressure was applied at room temperature before installation of the DAC stage into the cryostat and monitored by the ruby fluorescence at room temperature before and after the NIS studies. We observed minor pressure changes within 0.3 GPa between the before and after measurements due to cycling of the temperature in between and time-dependent pressure creep. Cooling from room temperature to low temperature may increase the pressure. However, additional compression results in irreversible gasket deformation, and the process of the pressure increase upon cooling is usually also irreversible. Thus, we would see a residual increase in pressure after warming up. Since our starting and final pressures, namely, before and after cooling, are within a range of 0.3 GPa, the pressure at the low temperature would be within 0.3 GPa of the pressure before cooling.

In addition to the NIS experiment, nuclear forward scattering (NFS) and Raman studies were performed. We used the

Figure 4
The setup of the high-pressure DAC stage, together with a cryostat without (inset) and with a cryostat cap. Red arrows show the beam incident on the BSM (dashed arrow) and the reflected beam (solid arrow) with a gap of 20 mm between the two beams. The yellow arrow indicates the Kapton windows in front of which the APD detector was installed.

Figure 5
The ^{125}Te NIS spectrum of TeO$_2$ measured at 5.5 (3) GPa and 25 (1) K. The blue open circles represent the instrumental function scaled down by a factor of 5.

Figure 6
^{125}Te NFS time spectra of TeO$_2$ measured at ambient pressure and room temperature (top), and at 5.5 (3) and 8.4 (3) GPa (centre and bottom), together with the NIS measurements. The red curves show fits using the quadrupole hyperfine interaction and the sample thickness.

Raman system installed on the PETRA III Extreme Conditions Beamline P02.2 and Extreme Conditions Science Infrastructure (ESCI) (Liermann *et al.*, 2015). We employed a 532 nm wavelength laser with a power of ∼40 mW focused on the sample, an Andor Shamrock SR-500i-A spectrometer equipped with a DU940P-BV CCD camera and a grating with a period of 1800 lines mm^{-1}.

The ^{125}Te NIS spectrum of TeO$_2$ at 5.5 (3) GPa is shown in Fig. 5. The total measurement time was ∼5 h. The detailed thermal balance of the negative and positive parts of the spectrum evaluated with Bose–Einstein statistics yields a sample temperature of 25 (2) K.

The NFS time spectra measured on the sample at ambient pressure, 296 K and under the conditions of the NIS measurements are shown in Fig. 6. A model using a quadrupole hyperfine interaction and the sample thickness gives reasonable agreement with the measurements. The quadrupole splitting decreases slightly with pressure as shown in the inset to Fig. 6. The ambient-pressure value of the quadrupole splitting agrees well with the results reported by Jung & Triftshäuser (1968) and Klobes *et al.* (2014).

The ^{125}Te PDOS evaluated from the NIS spectra are shown in Fig. 7. For the purpose of this discussion, we reproduce here also the PDOS previously measured at ambient pressure (Jafari, 2016).

In order to take into account the asymmetry of the instrumental function which gives an artificial shift of the PDOS peaks, the data treatment includes a deconvolution of the NIS spectra with the instrumental function and convolution by a Gaussian with a 2 meV FWHM. The convolution with a Gaussian was used here to suppress high-frequency noise appearing due to the deconvolution. Because of the fast decay of the Gaussian tails, the artificial 2 meV frequency oscillations are present in the spectra.
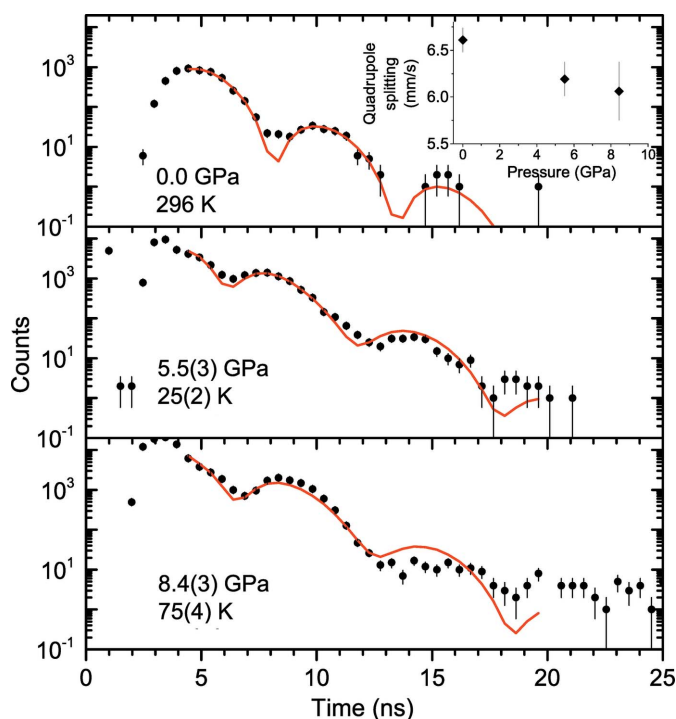
The Raman peaks evaluated from the Raman spectra measured on the sample at room temperature and the corresponding pressures are shown in Fig. 7 together with the PDOS. The Raman spectra were filtered at 130 cm^{-1} by a notch filter. The positions of the Raman peaks here agree well with the results reported by Kourouklis & Jayaraman (1992).

The PDOS at ambient pressure includes a pronounced peak at 10 meV, which corresponds to the van Hove singularity of the acoustic phonon branches, as well as a set of optical phonon peaks with well resolved energies at 19–24 and 27 meV. Compression leads to hardening of the PDOS and the Raman peaks in a similar manner. The effect of the compression on lattice dynamics parameters, such as the Lamb–Mössbauer factor, mean sound velocity and displacement parameters, are shown in Table 1. The phonon hardening is nearly proportional to the applied pressure. The parameters and peak positions change by ∼8% at 5.5 (3) GPa and by ∼12% at 8.4 (3) GPa relative to those at ambient pressure.

The evolution of the acoustic part of the PDOS under compression is seen in the inset to Fig. 7 where PDOS/E^2 is shown. The data at high pressure show a flat behaviour with straightforward extrapolation of the Debye level up to 0 meV, which is used to calculate the mean sound velocity. On the other hand, the ambient-pressure PDOS shows peaks in PDOS/E^2 at 3 and 9 meV which are due to the very soft phonon modes in the ambient-pressure phase. Under these conditions, the extrapolation of the Debye level done here, leading to a mean sound velocity of 2.2 (1) km s^{-1}, could be debatable. A mean sound velocity of 1.91 km s^{-1} was obtained

Table 1
Parameters obtained from the PDOS of TeO_2 measured at the indicated pressures P and temperatures T: the Lamb–Mössbauer factor f_{LM}, the mean sound velocity $\langle v \rangle$, and the Te atomic displacement parameters U_{eq} calculated for $T = 0$ K and $T = 300$ K assuming harmonic phonon behaviour (negligible PDOS change with temperature); U_{eq}^{th} shows the Te atomic displacement parameters obtained from theoretical calculations.
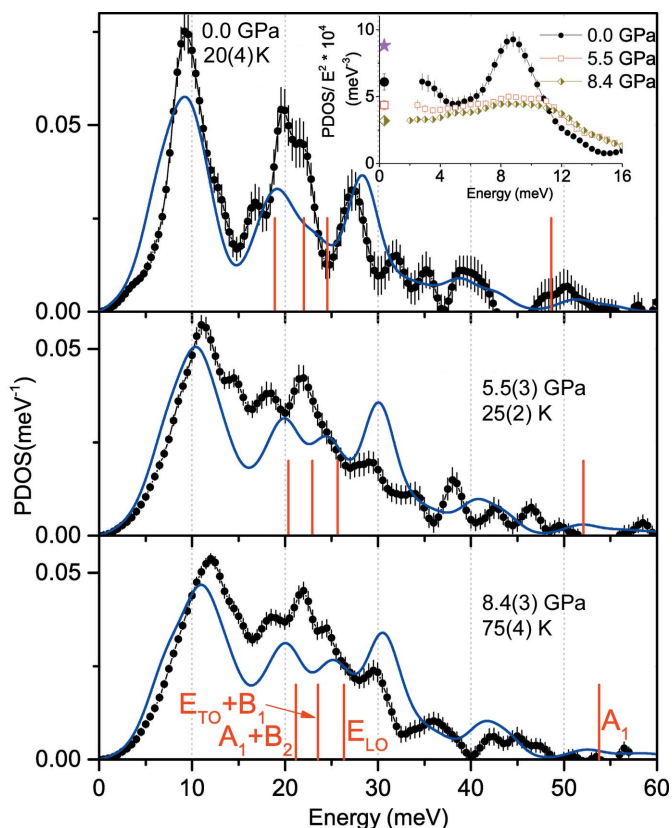
P (GPa)	T (K)	f_{LM}	$\langle v \rangle$ (km s^{-1})	U_{eq} (pm^2)		U_{eq}^{th} (pm^2)	
				0 K	300 K	0 K	300 K
0.0	20 (4)	0.645 (6)	2.20 (10)	12.4 (3)	81.3	12.40	81.48
5.5 (3)	25 (2)	0.665 (3)	2.38 (7)	11.4 (2)	66.3	11.06	62.88
8.4 (3)	75 (4)	0.567 (3)	2.54 (5)	11.1 (2)	61.2	10.62	57.41

by Ogi *et al.* (2004), leading to the significantly higher Debye level shown in the inset to Fig. 7. The increase in the Debye level is most probably related to the phase transition and a subsequent change in the acoustic modes.

The measurements were complemented by calculations of the phonon dispersions and corresponding PDOS (Fig. 7) of orthorhombic TeO_2 at $P = 0$, 5.5 and 8.4 GPa from density functional theory as implemented in *VASP* (Kresse & Furthmüller, 1996). Calculations were derived from the
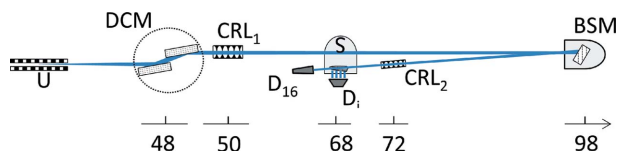

Figure 7
The Te PDOS of TeO_2 measured at the indicated pressures and temperatures. The blue curves show the calculated Te PDOS of orthorhombic TeO_2 at the corresponding pressures. The red vertical lines denote the positions of the Raman peaks measured on the same sample at room temperature and the corresponding pressures. The inset shows the reduced PDOS (PDOS/E^2), with the points at zero energy denoting the extrapolated Debye levels. The magenta star shows the Debye level calculated using the mean sound velocity obtained by Ogi *et al.* (2004).

PBEsol exchange/correlation functional (Perdew *et al.*, 2008) and PAW pseudopotentials (six valence electrons for each element) (Blöchl, 1994; Kresse & Joubert, 1999). The orthorhombic TeO_2 structure was relaxed (forces < 10^{-3} eV Å^{-1}) using a k-point grid $4 \times 2 \times 4$ to give optimized lattice parameters $a = 5.33$, $b = 11.81$ and $c = 5.70$ Å, in reasonable agreement with measured values (Ito & Sawada, 1940). To simulate pressure, this ground-state structure was hydrostatically compressed and the atomic positions relaxed to a new equilibrium. Within the pressure range investigated here, a decreased monotonically with pressure (as expected), while b and c decreased initially and then increased slightly upon further increasing the pressure: $P = 5.5$ GPa gave $a = 4.99$, $b = 11.47$ and $c = 5.67$ Å; $P = 8.4$ GPa gave $a = 4.80$, $b = 11.48$ and $c = 5.69$ Å.

For all cases, interatomic force constants (necessary for calculations of phonons and related properties) were obtained using the finite displacement method in the *PHONOPY* package (Togo & Tanaka, 2015) using $3 \times 2 \times 3$ supercells (432 atoms) and Γ-point-only calculations. The PDOS was calculated on a dense q-point mesh and using Gaussian broadening with a 2 meV width similar to that used to represent the measured data (Fig. 7). We note that PDOS calculations at ambient pressure for different TeO_2 polymorphs and including dispersion corrections were presented by Deringer *et al.* (2014). The general Te PDOS features correlate well with the measured data, namely, the peak positions, and the hardening and broadening of the peaks with pressure. The calculated Te atomic mean-squared displacement parameters at 0 and 300 K are shown in Table 1 and demonstrate good agreement with the measured values.

5. Results and discussion

The experiments performed in this study illustrate the capability to perform ^{125}Te NIS experiments up to 10 GPa at temperatures below 100 K, and, furthermore, they demonstrate that it is possible to obtain a Te PDOS under these conditions.

The setup used for this study can also be utilized to perform ^{121}Sb NIS experiments since the nuclear resonance energy of ^{121}Sb (37.1 keV) is quite close to that of ^{125}Te. An Sb NIS study at ambient pressure and low temperature has already been performed on the beamline (Herrmann, 2019).

A disadvantage of the experimental setup presented in this work is the rather large beam size at the BSM and at the sample position. A decrease in the beam size at the BSM to 0.3 mm × 0.3 mm would significantly improve the energy resolution (Sergueev *et al.*, 2011; Jafari *et al.*, 2017). Furthermore, a decrease in the beam size at the sample position is important in order to increase the pressure range. Samples placed in diamond anvils with a culet size of 400 μm can be compressed up to ~20 GPa, and with a size of 100 μm beyond 100 GPa. Moreover, to perform measurements under quasi-hydrostatic conditions, the sample must be enclosed by a hydrostatic pressure-transmitting medium. In this case, a reasonable sample size must be of the order of 50 μm or lower.

Figure 8
A possible future experimental setup, with the beam focusing at the BSM at the first stage and at the sample (S) at the second stage. The elements here are the same as in Fig. 1. CRL_1 and CRL_2 are rotationally parabolic Be compound refractive lenses which focus the beam at the BSM and at the sample, respectively.

One should remark that experiments with beams larger than the sample are still possible, since NIS is an element-specific technique. There would be no signal yield from the Be gasket, pressure medium or diamonds, which do not contain the studied isotope. However, the signal would decrease significantly and thus make data acquisition more time consuming.

An improvement of the setup would require modifying the focusing optics in order to reach a smaller beam size at the BSM and a beam size less than or equal to 50 μm at the sample position without having strong absorption effects. The optimal setup with two sets of CRLs is shown in Fig. 8. Here, a first set of rotationally parabolic Be CRLs (CRL_1) focuses the beam at the BSM with an almost one-to-one ratio of the distances from the CRLs to the X-ray source and to the image. The focal length of the CRL is 25 m. This CRL can be constructed using 15 CRLs with radii of 200 μm and geometric apertures of 0.9 mm. The beam size at the BSM will then be the same as the source size, *i.e.* 25 μm × 330 μm (V × H). The second set of rotationally parabolic Be CRLs (CRL_2) focuses the beam at the sample position with a ratio of 1:6.5, leading to a theoretical beam size at the sample position of 4 μm × 50 μm (V × H). This CRL has a focal length of 3.5 m and can be constructed using 27 CRLs with radii of 50 μm and geometric apertures of 0.4 mm. Importantly, due to the large distance between the BSM and CRL_2, the distance between the incident and reflected beams would have to be of the order of 20 mm, which provides enough space for the CRL_2 installation. The total transmission through both CRLs would be 0.33, which is comparable with the transmission of 0.5 of the current setup.

A further decrease in the focal size at the sample position is expected after the upgrade of PETRA III to the PETRA IV ultimate storage ring. This would lead to a significant decrease in the horizontal source size which will be comparable with the vertical size. Thus, the beam size at the sample position in the setup discussed above would be less then 10 μm in both directions.

6. Conclusions

The experimental setup described here demonstrates the principal capability to perform ^{125}Te NIS experiments under compression up to 10 GPa and at temperatures as low as 25 K. The method was applied to obtain partial Te phonon DOS of ^{125}TeO$_2$ at 5.5 (3) and 8.4 (3) GPa, which we compared with Raman spectroscopy data and with theoretical calculations. In

addition, the evolution of the hyperfine quadrupole splitting under pressure was measured by nuclear forward scattering.

The same method can be also applied to investigate ^{121}Sb nuclear resonance. A possible upgrade of the setup would extend the pressure range where measurements can be performed up to at least 100 GPa, covering a wide range of fundamental and applied science applications with ^{125}Te and ^{121}Sb nuclear isotopes.

Here we have also reported the new development of a miniature panoramic diamond-anvil cell and its application to low-temperature NIS studies. Due to the geometry of the backscattering, its small dimensions played a crucial role. At the same time the cell can be used with less complicated setups, *e.g.* with other nuclear resonances which do not require a BSM, such as ^{57}Fe, ^{119}Sn, ^{151}Eu, ^{149}Sm or ^{161}Dy. In addition, the same cell can be used for other synchrotron techniques, like X-ray emission spectroscopy, X-ray absorption near-edge structure (XANES), extended X-ray absorption fine structure (EXAFS) and X-ray diffraction (*e.g.* in the radial regime, perpendicular to the compression axis). Finally, the optimized dimensions of the cell and the low-friction area between the cylinder and the piston may be advantageous for dynamic compression experiments in the radial geometry at synchrotron and free-electron laser facilities.

References

Alexeev, P., Asadchikov, V., Bessas, D., Butashin, A., Deryabin, A., Dill, F.-U., Ehnes, A., Herlitschke, M., Hermann, R. P., Jafari, A., Prokhorov, I., Roshchin, B., Röhlsberger, R., Schlage, K., Sergueev, I., Siemens, A. & Wille, H.-C. (2016). *Hyperfine Interact.* **237**, 59.

Bauer Pereira, P., Sergueev, I., Gorsse, S., Dadda, J., Müller, E. & Hermann, R. P. (2013). *Phys. Status Solidi B*, **250**, 1300–1307.

Bessas, D., Sergueev, I., Wille, H.-C., Perßon, J., Ebling, D. & Hermann, R. P. (2012). *Phys. Rev. B*, **86**, 224301.

Bi, W., Zhao, J., Lin, J.-F., Jia, Q., Hu, M. Y., Jin, C., Ferry, R., Yang, W., Struzhkin, V. & Alp, E. E. (2015). *J. Synchrotron Rad.* **22**, 760–765.

Blöchl, P. E. (1994). *Phys. Rev. B*, **50**, 17953–17979.

Chumakov, A. & Sturhahn, W. (1999). *Hyperfine Interact.* **123/124**, 781–808.

Deringer, V. L., Stoffel, R. P. & Dronskowski, R. (2014). *Cryst. Growth Des.* **14**, 871–878.

Herrmann, M. G. (2019). Manuscript in preparation.

Ito, T. & Sawada, H. (1940). *Z. Kristallogr. Cryst. Mater.* **102**, 13.

Jafari, A. (2016). *Sapphire Ultraoptics for Sub-meV ^{121}Sb and ^{125}Te Phonon Spectroscopy.* Doctoral thesis, Université de Liège, Belgium.

Jafari, A., Sergueev, I., Bessas, D., Klobes, B., Roschin, B. S., Asadchikov, V. E., Alexeev, P., Härtwig, J., Chumakov, A. I., Wille, H.-C. & Hermann, R. P. (2017). *J. Appl. Phys.* **121**, 044901.

Jung, P. & Triftshäuser, W. (1968). *Phys. Rev.* **175**, 512–521.

Klobes, B., Barrier, N., Vertruyen, B., Martin, C. & Hermann, R. P. (2014). *Hyperfine Interact.* **226**, 713–719.

Klobes, B., Desmedt, A., Sergueev, I., Schmalzl, K. & Hermann, R. P. (2013). *Europhys. Lett.* **103**, 36001.

Kondratyuk, I. P., Muradyan, L. A., Pisarevskii, Y. V. & Simonov, V. I. (1987). *Kristallografiya*, **32**, 609–617.

Kourouklis, G. A. & Jayaraman, A. (1992). *High. Press. Res.* **9**, 23–26.

Kresse, G. & Furthmüller, J. (1996). *Comput. Mater. Sci.* **6**, 15–50.

Kresse, G. & Joubert, D. (1999). *Phys. Rev. B*, **59**, 1758–1775.

Ksenofontov, V., Wortmann, G., Chumakov, A. I., Gasi, T., Medvedev, S., McQueen, T. M., Cava, R. J. & Felser, C. (2010). *Phys. Rev. B*, **81**, 184510.

Liermann, H.-P., Konôpková, Z., Morgenroth, W., Glazyrin, K., Bednarčik, J., McBride, E. E., Petitgirard, S., Delitz, J. T., Wendt, M., Bican, Y., Ehnes, A., Schwark, I., Rothkirch, A., Tischer, M., Heuer, J., Schulte-Schrepping, H., Kracht, T. & Franz, H. (2015). *J. Synchrotron Rad.* **22**, 908–924.

Lindqvist, O., Haaland, A., Nilsson, J. E., Gronowitz, S., Christiansen, H. & Rosén, U. (1968). *Acta Chem. Scand.* **22**, 977–982.

Liu, L. G. (1987). *J. Phys. Chem. Solids*, **48**, 719–722.

Matsunaga, T., Yamada, N., Kojima, R., Shamoto, S., Sato, M., Tanida, H., Uruga, T., Kohara, S., Takata, M., Zalden, P., Bruns, G., Sergueev, I., Wille, H. C., Hermann, R. P. & Wuttig, M. (2011). *Adv. Funct. Mater.* **21**, 2232–2239.

Mizuguchi, Y. & Takano, Y. (2010). *J. Phys. Soc. Jpn*, **79**, 102001.

Ogi, H., Fukunaga, M., Hirao, M. & Ledbetter, H. (2004). *Phys. Rev. B*, **69**, 024104.

Parshin, P. P., Chumakov, A. I., Alekseev, P. A., Nemkovski, K. S., Perßon, J., Dubrovinsky, L., Kantor, A. & Rüffer, R. (2016). *Phys. Rev. B*, **93**, 081102.

Perdew, J. P., Ruzsinszky, A., Csonka, G. I., Vydrov, O. A., Scuseria, G. E., Constantin, L. A., Zhou, X. & Burke, K. (2008). *Phys. Rev. Lett.* **100**, 136406.

Sergueev, I., Glazyrin, K., Kantor, I., McGuire, M. A., Chumakov, A. I., Klobes, B., Sales, B. C. & Hermann, R. P. (2015). *Phys. Rev. B*, **91**, 224304.

Sergueev, I., Wille, H.-C., Hermann, R. P., Bessas, D., Shvyd'ko, Y. V., Zajac, M. & Rüffer, R. (2011). *J. Synchrotron Rad.* **18**, 802–810.

Seto, M., Yoda, Y., Kikuta, S., Zhang, X. W. & Ando, M. (1995). *Phys. Rev. Lett.* **74**, 3828–3831.

Shvyd'ko, Y. & Gerdau, E. (1999). *Hyperfine Interact.* **123/124**, 741–776.

Simon, R. E., Sergueev, I., Kantor, I., Kantor, A., Perßon, J. & Hermann, R. P. (2014). *Semicond. Sci. Technol.* **29**, 124001.

Snyder, G. J. & Toberer, E. S. (2008). *Nat. Mater.* **7**, 105–114.

Sturhahn, W., Toellner, T. S., Alp, E. E., Zhang, X., Ando, M., Yoda, Y., Kikuta, S., Seto, M., Kimball, C. W. & Dabrowski, B. (1995). *Phys. Rev. Lett.* **74**, 3832–3835.

Thomas, P. A. (1988). *J. Phys. C Solid State Phys.* **21**, 4611–4627.

Togo, A. & Tanaka, I. (2015). *Scr. Mater.* **108**, 1–5.

Wille, H.-C., Franz, H., Röhlsberger, R., Caliebe, W. A. & Dill, F.-U. (2010b). *J. Phys. Conf. Ser.* **217**, 012008.

Wille, H.-C., Hermann, R. P., Sergueev, I., Pelzer, U., Möchel, A., Claudio, T., Perßon, J., Rüffer, R., Said, A. & Shvyd'ko, Yu. V. (2010a). *Europhys. Lett.* **91**, 62001.

Wille, H. C., Shvyd'ko, Y. V., Alp, E. E., Rüter, H. D., Leupold, O., Sergueev, I., Rüffer, R., Barla, A. & Sanchez, J. P. (2006). *Europhys. Lett.* **74**, 170–176.

Worlton, T. G. & Beyerlein, R. A. (1975). *Phys. Rev. B*, **12**, 1899–1907.

Wuttig, M. & Yamada, N. (2007). *Nat. Mater.* **6**, 824–832.

Zhang, D., Jackson, J. M., Chen, B., Sturhahn, W., Zhao, J., Yan, J. & Caracas, R. (2013). *J. Geophys. Res. Solid Earth*, **118**, 4071–4082.

Zhao, J., Sturhahn, W., Lin, J., Shen, G., Alp, E. E. & Mao, H. (2004). *High. Press. Res.* **24**, 447–457.

Zhao, J. Y., Bi, W., Sinogeikin, S., Hu, M. Y., Alp, E. E., Wang, X. C., Jin, C. Q. & Lin, J. F. (2017). *Rev. Sci. Instrum.* **88**, 125109.